Search for OH Megamasers at redshift z $\sim$ 1.7 in the GOODS-North Field

A thesis submitted towards partial fulfilment of

BS-MS Dual Degree Programme

by

PALLAVI PATIL

under the guidance of

Dr. ramana athreya

Indian Institute of Science Education and Research

Pune

Certificate

This is to certify that this thesis entitled **"Search for OH Megamasers at redshift z $\sim$ 1.7 in the GOODS-North Field"** submitted towards the partial fulfilment of the BS-MS dual degree programme at the Indian Institute of Science Education and Research-Pune represents original research carried out by **Pallavi Patil** at Indian Institute of Science Education and Research-Pune, under the supervision of **Dr. Ramana Athreya** during the academic year 2013-2014.

Student

PALLAVI PATIL

Supervisor

RAMANA

ATHREYA

Acknowledgements

I owe my deepest gratitude to Ramana Athreya, my thesis supervisor, for providing me the golden oppoturnity to work with him. This project could not have been possible without his continuos support, motivation and insightful discussions. I am very fortunate to have him as my mentor.

I would also like to thank my friends and families for their undivided support and encouragement. I sincerely thank IISER Pune for providing me this wonderful platform to explore science on my own. It was a great learning experience.

Abstract

OH Megamasers (OHMs), including four spectral lines at 1.6 GHz, arise in the central dust torus of a galaxy. OHMs trace several astrophysical processes; they: (i) signal a specific stage in the merger process of gas rich galaxies. (ii) are useful in determining extragalactic magnetic fields, and (iii) signpost galaxies with extreme star formation. They are rare phenomena in the local universe, but are expected to be more luminous and more numerous in the distant universe at z = 1-2. However, sensitivity and radio frequency interference (RFI) at low frequencies are the major limiting factors for surveys of distant OHMs.

International efforts have come together to generate multi-wavelength data on particular regions in the sky free from contamination by strong Galactic sources. It is now possible to carry out comprehensive studies of the distant, and hence early, Universe by comparing the properties of sources across the entire electromagnetic spectrum. Great Origins Observatory Survey (GOODS) is such an effort which has generated data in two celestial regions (one each in the Northern and Southern hemisphere) at wavelengths ranging from radio to X-ray.

The GOODS-North field was observed for 5 nights at 610 MHz during May and June, 2009, using the Giant Meterwave Radio Telescope (GMRT). Our aim in this project is to detect OHM emission at redshift z $\sim$ 1.7 in the GOODS-North field. The analysis of the data was done using the software package AIPS (Astronomical Image Processing System) developed by NRAO, and in-house tools developed for RFI excision and high sensitivity imaging.

We have reached close to the required image noise of 10μJy, which is among the best currently achieved anywhere. We are addressing some image analysis issues to improve the image sensitivity further. The detection of megamasers at high

redshifts will open the doors to a variety of studies of the early Universe. Since, the maser phenomenon is predicted to be stronger and more numerous at high redshift, even the lack of detection will be an important input into the models of galaxy evolution.

Contents

Chapter 1

An overview of Maser

1.1 Introduction

Maser is an acronym for Microwave Amplification by Stimulated Emission of Radiation. Masers are narrow, intense molecular emission lines observed in a wide variety of extraterrestrial environments under special conditions. OH and H_2O were the first two molecules to be detected in maser emission from HII regions [43, 10] . Further observations led to the discovery of SiO [40], CH_3OH [4], NH_3 [23] masers. Masers are associated with comets [5], star forming regions [32], circumstellar envelopes around evolved stars [7] as well as the circumnuclear disks in Active Galactic Nuclei (AGN)[30] and starburst galaxies. The intense and narrow (high velocity resolution) emission lines provide a powerful tool to probe astrophysical conditions and processes that are difficult to study with other means[9]. Cosmic maser emission can be used to study the dynamics and kinematics of the molecular medium in which they originate and to measure distances with the great precision which is very important in establishing distance ladders [21]. Extragalactic masers are a million times more luminous than their galactic counterparts. H_2O and OH masers more abundant in extragalactic environments as compared to other

masing molecules.

Extragalactic masers operate under different physical conditions and are termed as Megamasers due to their very high spectral luminosity (typical megamaser has line luminosity $\sim 10^3 L_\odot$ whereas Galactic ones have $\sim 10^{-3} L_\odot$). They are excellent tools to probe the early Universe with great precision [27]. H_2O megamasers have provided evidence for the presence of black holes at the center of AGNs [29]. With the upcoming Square Kilometer Array (SKA) as well as with the present sensitive instruments, it should be possible to detect megamasers up to redshift of z $\sim$ 2 [27]. Such a detection will give us an independent tool to test the cosmological models and to study the galaxy formation and evolution in the early Universe.

1.2 Radiative transfer and Maser emission

Spontaneous emission, absorption and stimulated emission are three basic processes through which energy is transferred radiatively. The basic equation of radiative transfer is

$$\frac{dI_\nu}{d\tau_\nu} = -I_\nu + S_\nu \tag{1.1}$$

where I_ν is the brightness or specific intensity of radiation (amount of energy carried by a beam of radiation per unit time per unit frequency and per unit cross-sectional area). τ_ν is the optical depth which is the measure of the absorption along the path length of the propagating beam. S_ν is called the Source function which is the ratio of the emission coefficient and the absorption coefficient. For a blackbody radiation under Rayleigh -Jeans limit($h\nu << kT$), the brightness can be simply expressed in terms of its brightness temperature, T_b.

$$I_\nu(T_b) = \frac{2k\nu^2}{c^2} T_b \tag{1.2}$$

Consider a system of atoms with two energy levels. At thermal equilibrium, the rate at which those atoms are excited through collisions is equal to the rate at which de-excitations take place. The population at each level follows Boltzmann distribution and hence the number density for upper and lower levels is given by

$$\frac{n_u/g_u}{n_l/g_l} \;=\; exp\left(-\frac{h\nu}{kT}\right) \tag{1.3}$$

Where, $h\nu$ is the energy difference between those two levels. When the density of atoms is sufficiently large, for all positive temperatures, the number of atoms in upper level will always be less than the lower energy level. Stimulated emission is the process in which an atom in the excited state emits radiatively when stimulated by external radiation. So, under thermal equilibrium, such radiation will get absorbed in the medium. If somehow population is inverted, meaning $\frac{n_u/g_u}{n_l/g_l} > 1$, then the absorption coefficient becomes negative. This makes amplification of the intensity of background radiation possible. Such a non-thermal equilibrium requires gas density to be less than a critical value to maintain the inverted population.

For the system let T_x be the excitation temperature, such that

$$\frac{n_2}{n_1} \;=\; exp\left(-\frac{h\nu}{kT_x}\right) \tag{1.4}$$

Expressing the absorption and emission coefficient in terms of Einstein coefficients and number densities, substituting them in the radiative transfer equation and using Eq.1.2 we get

$$T_b \;=\; T_x(1 - \; exp(-\tau)) \;+\; T_c \, exp(-\tau) \tag{1.5}$$

When the population is inverted, the absorption coefficient and hence, optical depth τ_ν becomes negative. From the equation above we can see that, if T_x is

constant then the brightness temperature will be exponential function of optical depth. So, the background radiation propagating through the medium will be amplified by the gain factor of $e^{|\tau|}$. This model explains the observed large brightness temperatures of maser emission lines.

Detectable maser emission is observed in the regions with sufficiently high gas density ($n(H_2)) \geq \ 10^7\ cm^{-3}$ (to provide adequate number of atoms such that the emission line luminosity is high and where the energy pumps can maintain the inverted population. The process of population inversion is called pumping. There are two mechanisms, radiative and collisional, through which pumping of maser can take place. Either way, molecules are excited to high energy states above the upper level involved in the maser transition. Then, excited molecules decay spontaneously to the upper level causing population inversion. As the radiation propagates through inverted medium, the background radiation is amplified over distance as large as a few parsecs[1]. This gives rise to very intense, narrow maser emission lines. The 22.235 GHz ($\lambda = 1.35cm$) H_2O maser transition operates with collisional pumping. Whereas the maser lines corresponding to the hyperfine transitions in an OH molecule takes place via radiative pumping. Protostars as well as young stars provide the necessary IR photons to excite OH radicals.

1.3 Maser transitions in water and Hydroxyl molecules

1.3.1 Water Maser

The H_2O molecule is like an asymmetric top with rotational transitions in the sub-millimeter and far-infrared wavelength range. The maser transition corresponds to a frequency of 22.235 GHz with $\lambda \ = 1.35cm$. This transition between rotational levels 6_{16} and 5_{23} results from collisional pumping. Maser emission between other

[1] 1 parsec(pc) = 3.2615 Light Years = 3.08 x 10^{16}m.

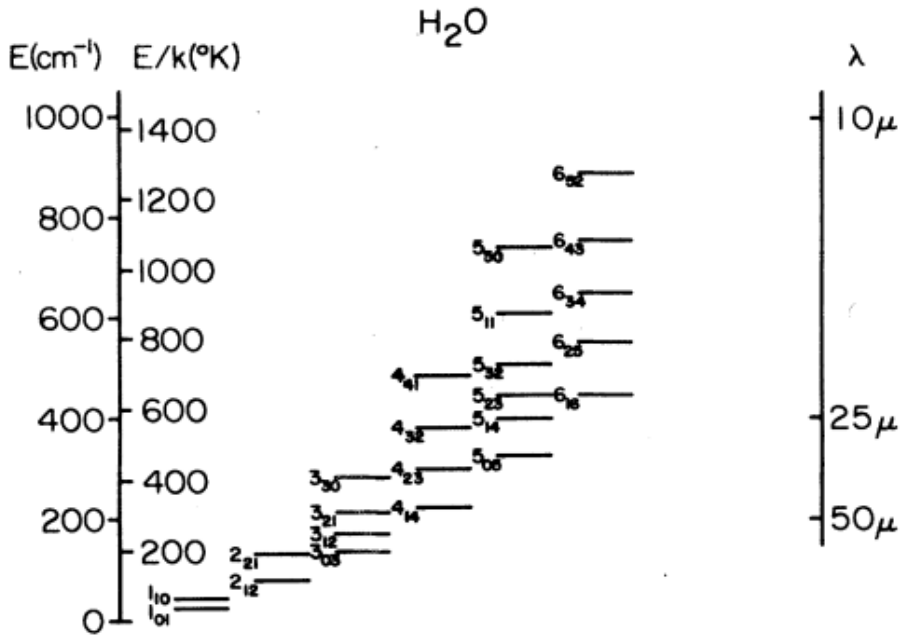

Figure 1.1: Fig.1 Rotational levels of H_2O molecules for $J \leq 6$. Each level is denoted by $J_{K_+K_-}$ J is total angular momentum and K_+ and K_- are it's projections on two molecular axes. The water maser transition involves 6_{16} and 5_{23} levels with frequency of 22 GHz and wavelength of about 1.35 cm. [18]

levels has also been observed but the 22 GHz radiation is present in all water masers. The water maser emission requires very dense gas ($10^7\, cm^{-3} < n(H_2) < 10^{11} cm^{-3}$) at the gas temperature of T > 300K.

1.3.2 Hydroxyl Maser

The hydroxyl radical is formed in the interstellar medium by the dissociation of H_2O molecule. It has an unpaired electron which is responsible for the maser transition between hyperfine components in the rotational ladder. The ground electronic state of OH radical is Π state which is split into two rotational ladders $^2\Pi_{3/2}$ and $^2\Pi_{1/2}$ due to coupling of electronic angular momentum and spin angular momentum. The energy levels are split into two unequal states due to interaction of electronic angular momentum and the rotational states. This is called Λ-splitting.

Λ doublets are further split into hyperfine components due to coupling of the spin of the unpaired electron with the nuclear spin of the H atom and are denoted by the quantum number F. The OH maser lines($\lambda = 18cm$) correspond to the transition between the hyperfine components of the ground rotational state of OH radical. The "main lines" with $\Delta F = 0$ are at frequencies 1665 MHz and 1667 MHz. Whereas, the OH lines with frequencies 1612 MHz and 1720 MHz are called "satellite lines" and have $|\Delta F| = 1$. The thermal strengths of those four lines are in ratio 1:5:9:1 for 1612, 1665, 1667, 1720 MHz respectively. The far-infrared emission coming intense starburst regions excites the electron to higher rotational states either in the same ladder or in the cross-ladder. This can invert population of different hyperfine components leading to either one or two emission lines. The physical conditions for OH maser requires less dense gas as compared H_2O with $10^4\ cm^{-3} <\ n(H_2)\ < 10^6 cm^{-3}$ and the temperature between 100K-300K. Thus, pumping of OH depends directly on the far-IR radiation. This relationship is an important marker in the search for maser candidates in the early Universe.

1.4 Galactic Masers

The first OH molecule was detected in absorption towards Cassiopeia A with the OH main line ratio comparable to the thermal ratio observed in the laboratory experiments.[44] The first emission was detected by Weaver et.al.[43] in W3 region from Orion and few other HII regions [43]. The emission features, which were called 'Mysterium' had unusual properties. The relative intensities of different OH lines were different than expected thermal ratios. Perkins et.al. [34] and Litvak et.al. [26] explained the observed emission characteristics of 'Mysterium' using maser amplification model. Very Long Baseline Interferometry (VLBI) observations of the maser sources by Moran et.al. [31] made it possible to determine the angular

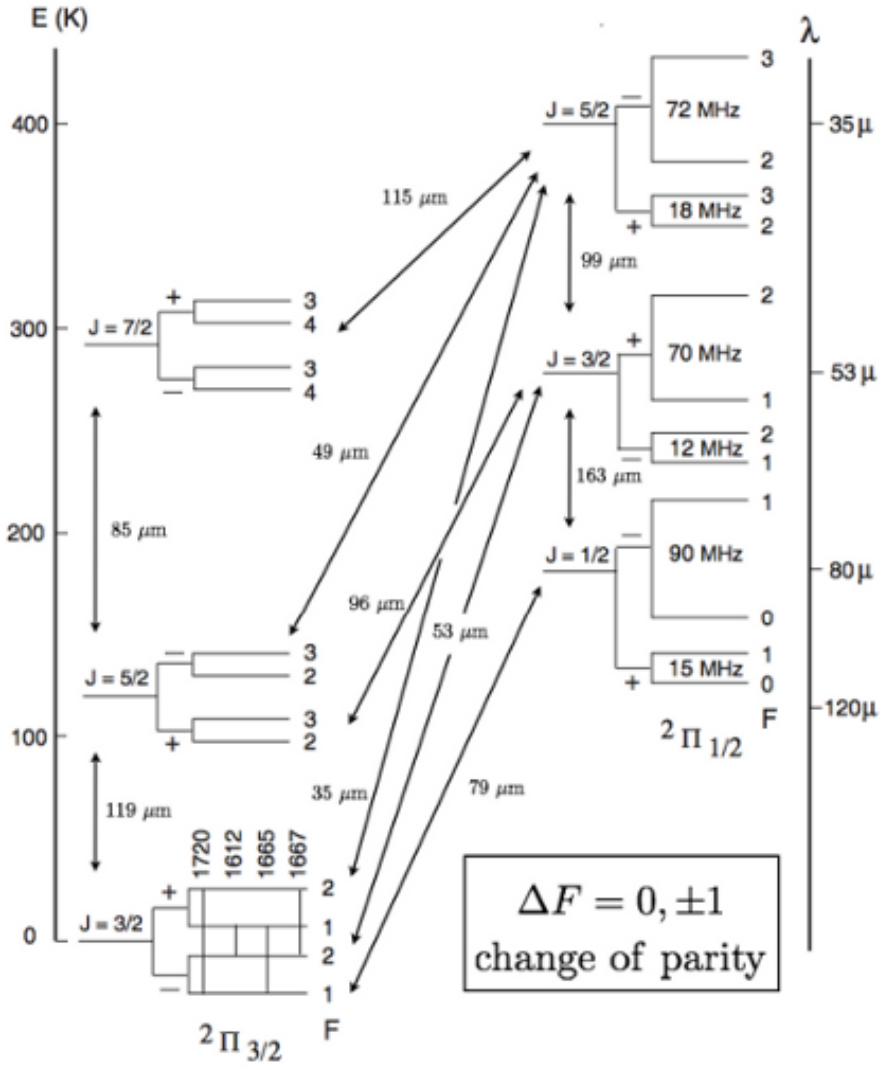

Figure 1.2: Energy diagram of OH molecule. The splitting among energy levels is not scaled. [46, 28]

size of emission sources and the brightness temperatures of such emission lines were estimated to be 10^{12} K. In 1969, Cheung et.al. [10] observed the water maser lines with line luminosity ranging from $10^{-3} - 1 L_{\odot}$ in a single emission line. Strong masers of SiO and CH_3OH are also found throughout the Galaxy.

Galactic masers are classified into two types based on their physical origin, interstellar and circumstellar. Interstellar masers are associated with star formation regions such as Ultra-compact HII regions, hot cores, protostellar disks and jets.[37]. Circumstellar masers are observed in the stellar envelopes of evolved stars such as red giant, supergiants and proto-planetary nebulae. The masing material for interstellar masers comes from the molecular clouds surrounding young stars or protostars whereas stellar masers arise from the material of the star itself.

Proper motion measurement of H_2O maser lines has enabled us to determine distances up to a large range.[19]. Also splitting of OH emission lines can be used to determine the magnetic field strengths near star formation region as well as evolved stars.[37]. The study of stellar masers has provided an insight into the evolution of late type of stars.

1.5 Extragalactic masers — Megamasers

Soon after the discovery of Galactic masers, a new type of extremely luminous (line luminosity was a million times higher than their Galactic counterparts) masers were discovered towards external galaxies. Hence, they were called Megamasers. The first megamaser was detected from water molecule in NGC 4945 [35]. Baan et.al. [3] detected first extragalactic OH megamaser emission in Arp 220 using Arecibo telescope. The VLA mapping of NGC 4258 and NGC 1068 constrained the location of masers within 1-3 pc from the nucleus and it was proposed that this emission must be originating from the molecular clouds surrounding the nucleus of

the host galaxy. [11] Various observations focused on NGC 4258 during 1984-1992 gave evidences in strong support of the model of circumnuclear maser model [27]. The study of water maser in NGC 4258 has provided direct observational evidence of the existence of a thin Keplerian molecular accretion disk in galactic nucleus, in strong support of long standing paradigm of accretion of matter by a super massive black hole to power quasars and AGNs [27]. The rotational curve study of maser emission provided strong constraints on the mass within 0.25 pc of the center of galaxy, thus constraining characteristics of the central black-hole. [29] Water masers are very useful for the determination of geometric distance. Maser surveys of active galaxies established that water megamasers are associated with the Seyfert2 and LINER AGNs. Megamaser cosmology project (MCP) is aimed at the search for H_2O megamasers with the hope of measuring Hubble constant as well distance determination and for precise measurement of mass of the black holes.[38, 8, 25, 39]

On the other front, hydroxyl megamasers are found to be mostly associated with LIRGs and ULIRGs with IR luminosity $L_{IR} \geq \ 10^{11} \ L_{\odot}$. The masers are known to be located within few hundred parsec from the center of galaxies and masing molecules are radiatively pumped from the IR radiation coming from regions of intense starburst activity. The luminosity of OH megamaser is correlated with IR luminosity with the relation $L_{OH} \propto \ L_{IR}^{1.2}$[14, 15, 16]. The upgraded Arecibo survey led to the detection of many new OH megamasers and the most distant OH megamaser was found at z= 0.265.[16]. The characteristics of OH megamaser are main line intensity ratio ($T_{1665MHz}/T_{1667MHz} > 1$), large linewidth ($> 100\ kms^{-1}$) and unpolarised emission. However, the IR-luminosity is not the only condition for the existence of OH megamaser.[13]. OHM are signposts of the most intense,compact and unusual modes of star formation in the local Universe. The association of OHMs with the bright IR-merger galaxies indicate that OHMS

are expected to be more numerous and intense(Gigamasers) at redshift $z \simeq 1-2$ coinciding with increased merger activity and star formation.[45].

1.6 Recent developments and open problems

Water and Hydroxyl masers are the most common masers in both extragalactic and Galactic environments. In a survey of masing galaxies, 6 of the total 51 surveyed show both OH and H_2O maser emission. Whereas, 33 galaxies host only water maser and 13 galaxies host only hydroxyl emission.[42]. A deep survey is required to study the apparent lack of detection of both molecules in the same object. Also the multi-wavelength study of maser host galaxies is needed to establish the correlation between water masers and the gas from which it originates. Water megamasers are found to be associated with X-ray absorbed sources. ([47]).

Another important use of megamasers is to provide a test for the variation of fundamental constants with epoch. Kanekar et.al[24] have used the complex structure of OH maser lines to constraint the variation of fundamental constants with time. They have found no variation till $\sim$ 6.5Gyr, half of the age of the Universe.

There are still many unanswered questions, such as determination of lifetime of megamasers and the low detection rate of water megamasers.[27]. Also, an overall understanding of the maser phenomenon and its place in the Unified standard model of AGN will be better served with more, and detailed, observations in radio loud AGNs. [41].

In this report, I present an attempt to detect OH megamaser at the redshift of z $\sim$ 1.76. If detected will provide a tool to probe the Universe at epoch of intense starburst activities. We have analyzed the data observed at 610 MHz using Giant Meterwave Telescope(GMRT), Pune. The target field is called GOODS-north. In

chapter 2, I have explained the detailed procedure of data analysis and synthesis imaging that we have performed using AIPS and tools developed in-house. I have also described various issues specific to low frequency image analysis in radio astronomy. In chapter 3, I have summarized the final images after analysis and the future plan for spectral analysis to search for maser lines.

Chapter 2

Image Analysis

2.1 Introduction

The target field, GOODS-North, is a part of Great Observatories Origins Survey (GOODS) [17]. This survey combines extremely deep observations from ground- and space-based observatories across the electromagnetic spectrum. The multi-wavelength studies is expected to provide us the complete picture of galaxies and track the formation and evolution of galaxies and active galactic nuclei (AGN). GOODS-north field (GNF) is centered around the Hubble deep field (North), also called the Chandra Deep Field (CDF). The survey includes observations from Spitzer (mid-far infrared), Hubble (optical, near infrared), Chandra (X-ray), XMM-Newton (X-ray) and Herschel (infrared).

Deep radio imaging can provide a probe to observe objects that are obscured at X-ray and optical wavelengths (e.g. Dust obscured AGN, sub-mm galaxies) [33]. To complement the deep observations, GNF was observed at 1.4GHz using the Very Large Array(VLA) [33] and at 610MHz using the Giant Meterwave Radio Telescope (GMRT), Pune. The GMRT is one of the most sensitive instruments at low radio frequencies.

The aim of low frequency observations is to study the high redshift Universe and objects with steep spectral index. In this report, we present an analysis of the deep 610MHz observations of GNF. It is centered at right ascension 12h36m49sec and declination $62°12'58''$.

In the rest of the chapter, I will explain the basics of synthesis imaging, the procedure of data reduction including calibration, imaging and data editing. Then, I will discuss various problems that limit the dynamic range of the image and some of the in-house software tools developed to correct for these errors.

2.2 Interferometry and synthesis imaging

The atmosphere is transparent to radio waves in the frequency range 10 MHz – 300 GHz. Radio astronomy started in 1930s when Carl Jansky observed signals coming from the direction of Milky Way.

The basic tool of observation in radio astronomy is a radio antenna. The resolution (the ability to separate close-by objects) and sensitivity (ability to detect faint objects) decide the quality of observations. The sensitivity of an antenna increases with its area. The resolution of an antenna in any direction is proportional to its dimension in that direction. Long wavelength radio waves require much larger apertures to achieve a resolution comparable to optical telescopes. Building large antennas is not feasible. High resolution can also be achieved by correlating the output of two antennas separated by a large distance. This arrangement provides a resolution equivalent to an antenna with a diameter equal to the separation.

A two element interferometer consists of two single dish antennas separated by some distance (termed *baseline*). The output voltages of the two are correlated to obtain the interferometer response. This correlated output is called the visibility of the baseline and it corresponds to a particular Fourier component of intensity

distribution of the sky region under observation. This relationship between the visibility and the intensity is given by the **van Cittert-Zernike** theorem:

$$V(u,v,w) \;=\; \int I(l,m)e^{-2\pi i(ul+vm+wn)}\,\frac{dldm}{\sqrt{1-l^2-m^2}} \tag{2.1}$$

where l, m, n are the direction cosines on the sky from the center of the field; the baseline coordinates u, v, w form an orthogonal system and are given by $u = \frac{x_2-x_1}{\lambda}$, $v = \frac{y_2-y_1}{\lambda}$ and $w = \frac{z_2-z_1}{\lambda}$; and (x_2, y_2, y_2) and (x_1, y_1, z_1) are coordinates of the two antennas. It may be noted that the antenna coordinates are specified with respect to the source direction, such that the w is along the direction of the source and u,v are in the plane perpendicular to it.

By measuring large number of visibilities of different (u,v,w), i.e. different baselines, one can in principle determine the intensity distribution on the sky. Large number of baselines can be measured by simultaneously measuring the electric field in an array of many antennas. Martin Ryle proposed a better technique called **Aperture synthesis**, which utilizes Earth's rotation to increase number of baselines. As Earth rotates, a given pair of antennas rotate through different values of (u,v,w) providing different visibilities.

If either $w = 0$ (array lies perpendicular to the direction of the source) or $n = 1$ ($l \ll 1$ and $m \ll 1$), the relationship reduces to a two-dimensional Fourier transform.

Giant Meterwave Radio Telescope(GMRT),Pune, is an interferometric array of 30 antennas of 45m diameter. These single dish antennas are arranged in Y shape to maximise the UV coverage. The array provides 435 visibilities for every time sample (2-16 second)

2.3 Data reduction and imaging

In optical astronomy, the lens of the telescope Fourier transforms incoming radiation and we get final image. In radio observations, the signal we measure is the intensity of electric field of the incoming radiation. Each step involved adds it's own noise in the output of correlator which results in the distortion of final image or increase in it's noise. The process of mapping (Fourier transform of visibilities) should incorporate corrections for such errors prior to Fourier transforming the visibility function. In the following subsection, I will explain the step-by step procedure that we have implemented to obtain final images. For analysis of the data, we have used a software called AIPS (Astronomical Image Processing System) developed by NRAO (nation Radio Astronomy Observatory) and in-house software tools which use AIPS tasks and C-programs.

2.3.1 Observations

The target field GOODS-North was observed for 5 days in May 2009 and June 2009. The details of observation are given in table 2.1. The data from each day were edited and calibrated individually. The final image was made after combining the final data products from all the days.

2.3.2 Radio Frequency Interference (RFI) Mitigation

Radio frequency interference is the major factor affecting interferometric image sensitivity at low frequencies. RFI creates oscillations with the fringe-stop period in the correlator output resulting in systematic ripples and high noise in the image plane. We are used the RfiX algorithm [1], which identifies such patterns and subtracts them from the data.

Table 2.1: Details of observations.

GMRT Project code	16_052
Position	RA : 12h 26m 49s Dec : 62° 12′ 58″
Observation dates	9, 11, 12 May 2009 22, 23 June 2009
Field area covered	1.93 deg^2
Center frequency	610.437 MHz
Bandwidth	32 MHz
Number of channels	256
Channel width	125kHz
Flux calibrator	3C286
Phase calibrator	1313+675
Integration time	2sec
Total integration time	33 hours (5 days combined)
RMS noise level (single day one sideband)	near phase center : 30μJy Edge of the field 28μJy

2.3.3 Initial Calibration

The true visibility function is the spatial correlation function of the electric fields measured at each antenna. Due to several reasons, the output may deviate from the true visibility. The role of calibration is to recover the true visibility from the observed visibility data [20]. Let $V_{ij}(t,\nu)^{obs}$ denote the observed visibility of antenna pair i,j at a time t and frequency ν and $V_{ij}^{true}(t,\nu)$ be the corresponding true visibility. The relationship between two can be written as (ignoring t and ν for the moment),

$$V_{ij}^{obs} \;=\; (G_{ij} + B_{ij})\, V_{ij}^{true} \;+\; \epsilon_{ij} + \eta_{ij} \tag{2.2}$$

where

G_{ij} is the antenna based complex gain ($G_{ij} = g_i g_j$).

B_{ij} is the baseline based complex gain

ϵ_{ij} is the baseline based offset and

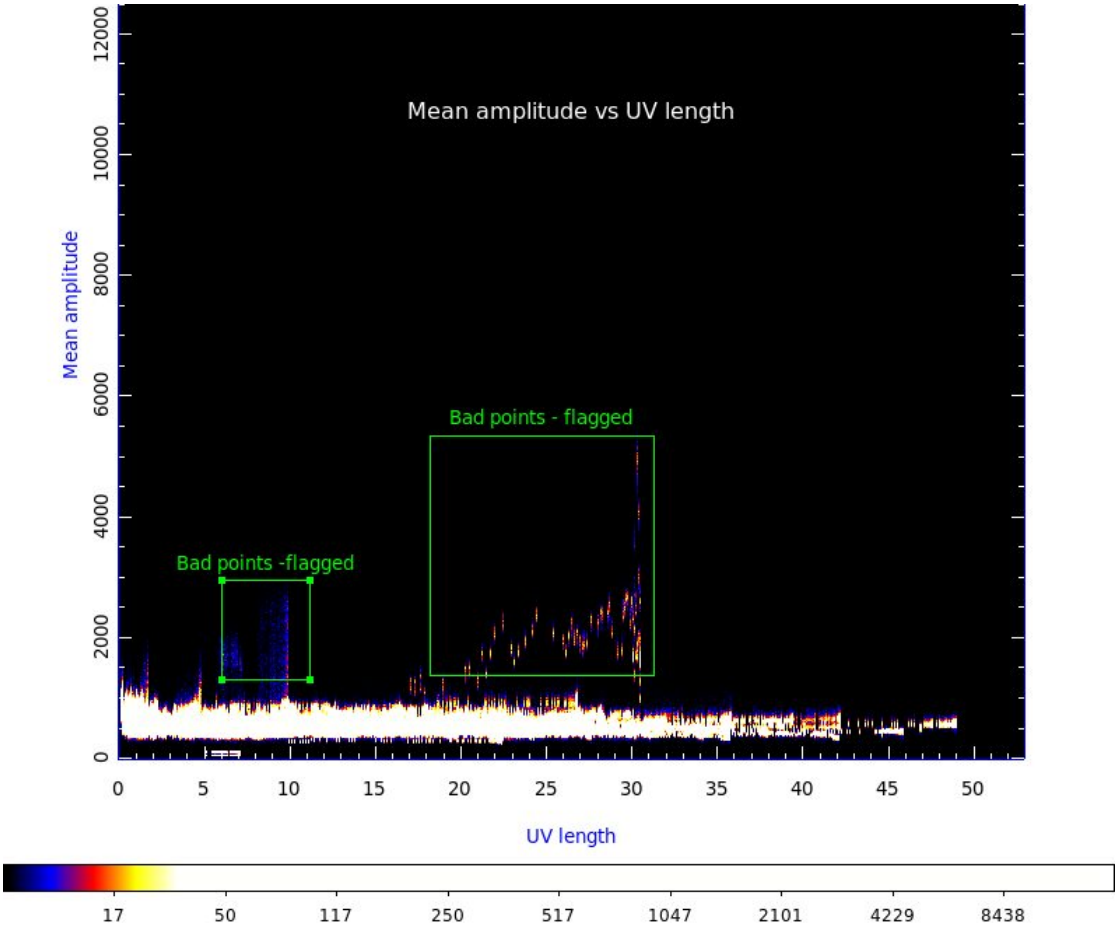

Figure 2.1: This the plot of mean amplitude vs uv length. Points in the boxes are obviously deviant from the good data.

η_{ij} is the random noise (receiver temperature and sky background). It may be noted that these quantities are function of time and frequency.

The goal of calibration is to estimate G_{ij}, B_{ij} and ϵ_{ij} parameters for each frequency and for all time t.

Bandpass calibration

Compensating for variation of gain across the bandwidth of observation is called "Bandpass Calibration". A strong, compact source with relatively flat spectral

index is observed to correct for the bandpass. In our case, the flux calibrator, 3C286, was used for this purpose.

After running the rfix algorithm on the 3C286 data for RFI mitigation (sec.2.3.3), the deviant visibilities were flagged — for a point source at the phase reference of antenna pointing, the amplitude and the phase should remain constant. We used the AIPS tasks BPASS and POSSM for bandpass calibration. We went through several iterations of bandpass calibration, imaging and data flagging before achieving the final bandpass calibration. Typically, at high frequencies, the bandpass calibration does not change over time. AIPS, which was largely developed for high frequencies does not allow for calibrating time variable bandpass. However, at low frequencies, the stronger effect of ionosphere and instrumental saturation due to RFI can result in a substantial variation of bandpass over time. We use our own software tool to compensate for this at a later stage (see under Self-calibration).

The bandpass calibration was applied prior to any analysis for each dataset.

Flux calibrator

An interferometer measures the relative amplitude of the complex visibilities. A celestial source with known, long term flux stability is observed at least once during every observation to estimate the absolute flux density scale of the visibilities. We observed 3C286 for flux calibration every 2 hours during each session. The standard flux density of 3C286 at the center frequency of the band was obtained using SETJY task in AIPS.

Phase Calibrator

The ionosphere can cause temporal variation in the phase of the incoming wavefront. Similarly, temporal variations in the receiver system can change both the amplitude and phase of the visibilities. Hence, a radio source with known structure

(usually an unresolved/point source) can be observed at regular intervals (every 15-60 minutes) to determine the temporal variation of complex gain. The phase calibrator should also be close to the target field to minimize differences due to variation of the complex gain across the atmosphere.

In this observation, 1313+675 was observed for phase calibration every 50 minutes.

2.3.4 Imaging and Self-calibration

The imaging was done with the task IMAGR. A circular synthesized beam of size $\sim$ 6 arcsec was used for imaging routine with the cell size of 1 arcsec. The field within 1.39 deg from phase center was imaged. The w term in Eq. 2.1 can only be assumed to be constant when the imaged area is small. However, at low frequency this assumption is no more valid and an additional phase term is introduced in Eq. 2.1 due to variation in the w-term. This effect is compensated by dividing the image into smaller facets (within which the change in w is small) and imaging each facet separately. The GNF was divided into 62 facets using SETFC. The 62 facets included 6 centered on the strongest sources, and the rest uniformly covering the entire primary beam.

The antenna-based complex gain $G_{ij}(t)$ can be divided into the individual antenna gains as ;

$$G_{ij}(t) \; = \; g_i(t) g_j^*(t) \tag{2.3}$$

where

$g_i(t)$ and $g_j(t)$are complex gain for antennas i and j respectively,

The phases and amplitudes of the observed visibilities follow relationships given below,

$$\phi_{12}^o \; + \phi_{23}^o \; + \phi_{31}^o \; = \; \phi_{12}^t \; + \phi_{23}^t \; + \phi_{31}^t \tag{2.4}$$

$$\frac{A^o_{12}A^o_{34}}{A^o_{23}A^o_{41}} = \frac{A^t_{12}A^t_{34}}{A^t_{23}A^t_{41}} \tag{2.5}$$

These are called closure relationships for phase and amplitudes respectively, where each visibility can be written as $V_{ij} = A_{ij}e^{i\phi_{ij}}$. An array with N_A antennas has N_A unknown phase gains. But it also has $N_B = N_A(N_A\text{-}1)/2$ baselines phases. These will yield $N_B(N_B\text{-}1)(N_B\text{-}2)/6$ closure phase relations. Clearly, this highly over-determined set of equations can be solved to obtain the unknown phase gains. Similarly, the unknown amplitude gains can also be solved.

Self-calibration is an algorithm which makes use of the above closure relations to create a series of incrementally improved images, by using a previous image to incrementally calibrate the next image.

In our analysis, we performed 5 iterations of selfcal and imaging with phase only calibration, and a final round of selfcal with amplitude calibration as well.

2.3.5 Decimation of data

To avoid corruption of large amount of data by RFI and for better elimination of RFI, the visibilities were sampled at 2 second intervals (instead of the usual 16 seconds). We also avoided permanently collapsing the 128 channels into a more manageable 10-20 channels (as is usually done) since we are interested in the detection of maser spectral line. This creates files with huge sizes ($\sim$ 50 GB for 8 hours of data). Handling of those files will take up lot of time and computational resources. We used a scheme by which imaging and self-calibration was done using a reduced data set (to increase computational speed) and yet be able to transfer the calibration parameter to the original high time- and frequency-resolution dataset.

The decimated data set is obtained by median filtering the visibilities within a grid of 5 frequency channels and 7 time integrations, reducing the file size by the factor of 35. The entire analysis including imaging, self-calibration, generating

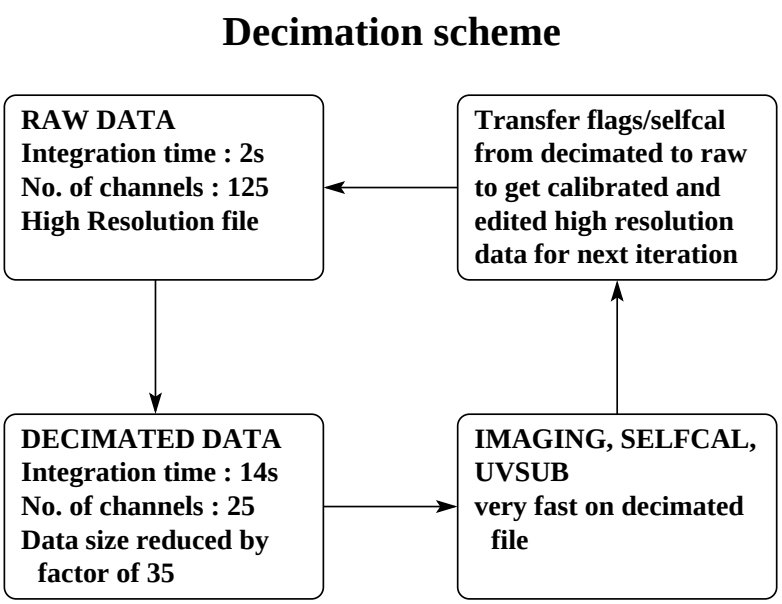

image model and flagging deviant data was done very efficiently on the decimated file. The calibration, model and data flags determined from the decimated data file were transferred back to the original file (2s integration, 128 channels). This method allowed us to save a lot of computational time without losing the sensitivity of the original data.

2.3.6 Analysis of residuals

In an ideal scenario, the residual image should have a featureless noise background, but any bad visibility data will lead to ripples in the image plane. Calibration errors and incorrect image models will create residual structures, especially around the strongest sources.

Bad visibility data may either be identified by inspecting the visibilities or by inferring their presence from structures in the image. In both cases, it would be best to work with residual data. The residual visibility data set is obtained by subtracting the model visibilities from the observed visibilities. The residual image is obtained by imaging the residual visibility data. The subtraction of a substantial

number of sources will bring the systematic errors in the residual visibilities/image into prominence, and make it easier to spot the corrupted data. If most of the flux from the strong sources is subtracted from the visibilities, the residuals will resemble thermal noise in the absence of systematic errors. Thus, any deviation which stands above thermal noise is almost certain to be systematic error.

Flagging Deviants in the Visibility Time-Channel Plot

We determined the local mean and standard deviation using a window on the time-channel plane of the visibilities of each baseline. Deviants were identified using the mean and standard deviation and flagged. The AIPS task TVFLG can carry out this procedure, but we have used a more efficient tool tailored to our needs.

Flagging Deviants in the UV plane

As Earth rotates, different baselines may occupy the same region in the u-v plane, though at different times. Nevertheless, the visibility measured by different baseline in the same u-v region must be the same.

Any transient contamination will only be present in the fraction of visibilities in that region and therefore, examining the visibilities within a small region in the u-v plane will help in identifying the contaminated data.

Additionally, we can identify regions in the u-v plane with bad data by comparing it with its neighboring regions. There is no equivalent task for this in AIPS. We used tools developed in-house for this purpose.

First, we gridded the residual visibilities in 100 X 100 λ squares in the UV plane. These were then plotted in semicircular strips of user specified widths (1000 λ) — See Fig. 2.2. One can easily spot the grids with deviant data, which stand out as bright spots in the plot. In the absence of systematic data corruption, one expects the distribution of the grid values to be featureless noise.

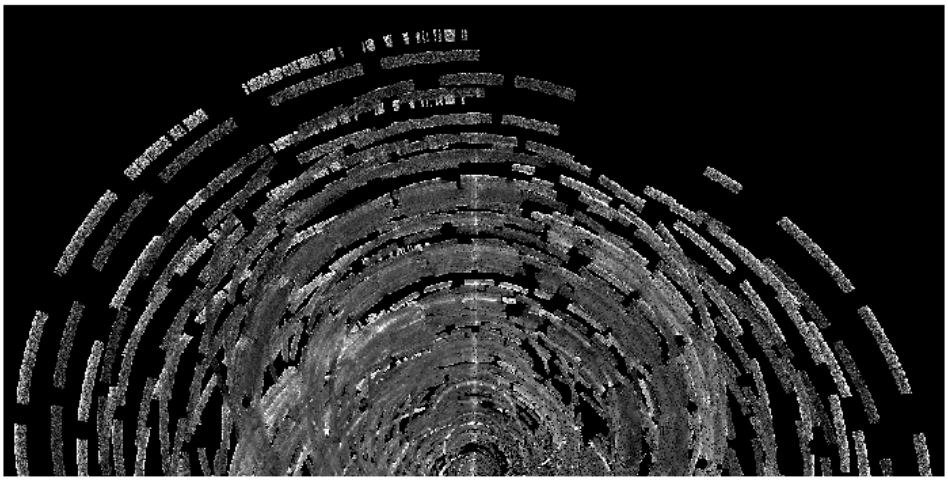

Figure 2.2: The UV-grid plot for the residual file. The bright points correspond to corrupted data. The histogram of points in one circular strip is shown above

Fig. 2.3 shows the histogram of grid values in one semicircular strip. The real and imaginary part of the residual visibility should follow zero mean Gaussian distribution and hence the amplitude should follow a Maxwelllian distribution. Corrupted data will add a long tail to the amplitude distribution which is clearly seen in the histogram.

We flagged the long tail of high amplitude beyond 0.2 Jy. This threshold was set by statistics of Maxwell distribution and the value of the histogram peak. The post flagging u-v plane is shown in Fig. 2.4.

The flags were transferred to the actual dataset and was reimaged and recalibrated. The residual visibilities with more correct calibration was further taken through the same procedure. Two or three rounds of flagging and recalibration has improved the image quality remarkably.

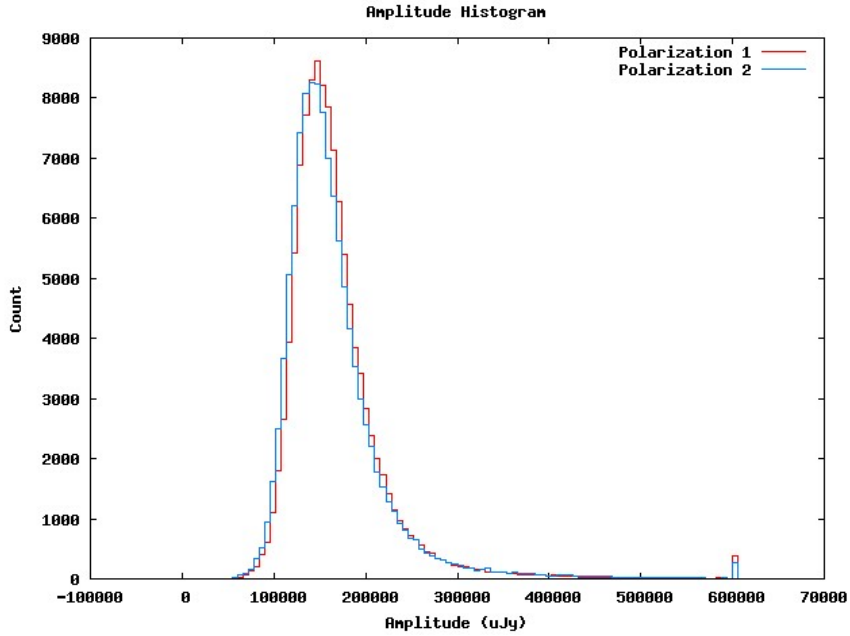

Figure 2.3: Amplitude histogram for one strip in the UV plane. The distribution is Maxwellian with a very long tail. We have flagged the tail above amplitude of 0.2Jy

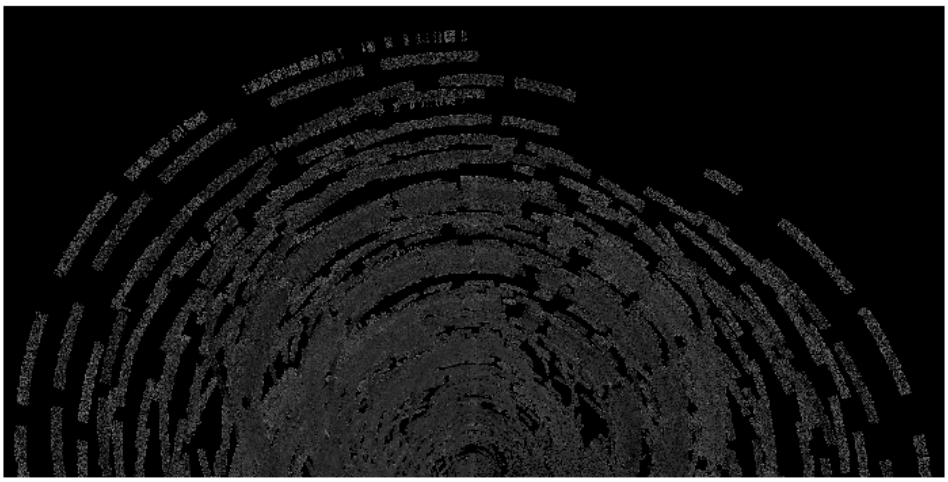

Figure 2.4: The UV-grid plot for residual file post flagging. The points are more or less noise like without any bright clumps of strips.

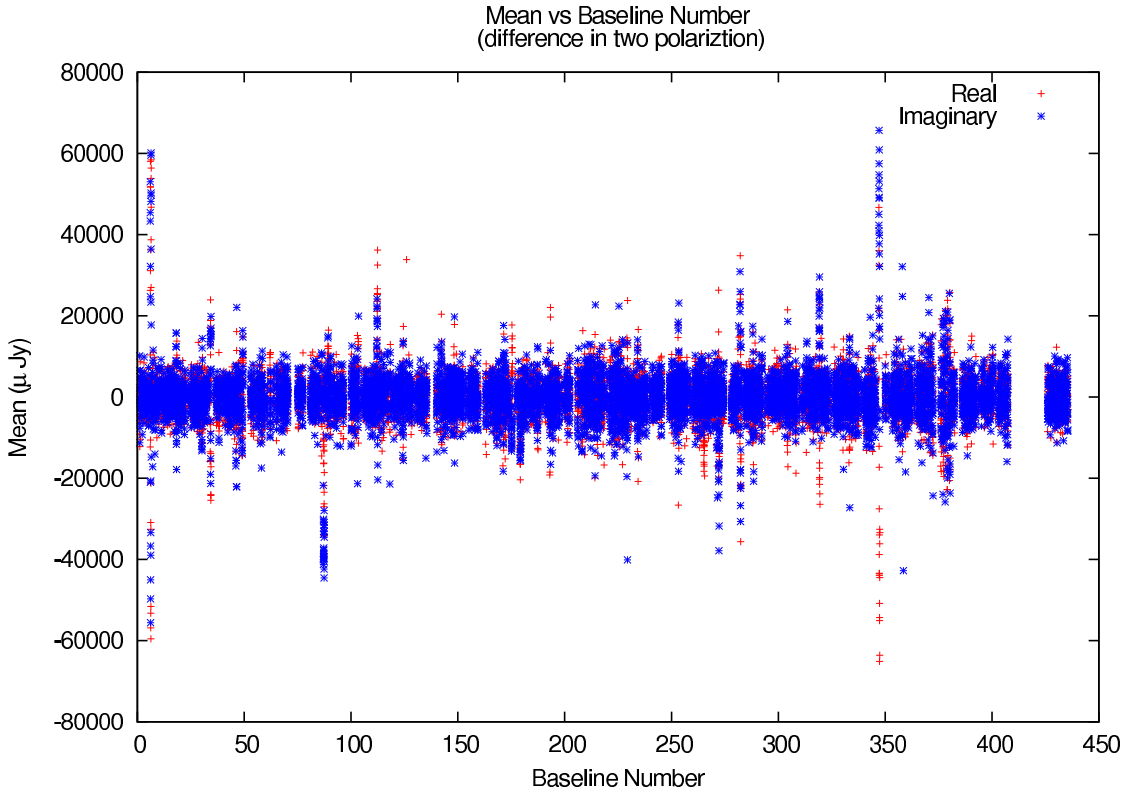

Figure 2.5: Plot of mean circular polarization (Right−Left) of baselines. The individual channels of each baseline occupy a single vertical strip. The red color is for real part and blue points are imaginary part of the visibilities. Most of the values cluster around zero as expected of good data. The deviant baselines are also obvious

2.3.7 Baseline corrections

Baseline offsets

The long term averages of real and imaginary values of residual visibilities are expected to be close to zero. Their deviation from zero will for all practical purposes will be a zero mean Gaussian, with a dispersion proportional to the system noise and inversely proportional to averaging time interval. Correlator errors can contribute an offset which can be detected only after such a long term average. Such

offsets will lead to gain calibration errors and ripples in the image plane, thus, limiting the dynamic range. We have developed a tool to identify and subtract such offsets.

As most astronomical signals have zero circular polarization, there should be no difference between the visibilities of right and left circular polarization. Therefore, the difference between two polarization should be noise-like, and any significant deviations from zero are likely to be due to systematic errors. We have taken median of real and imaginary part of visibilities separately over time for each baseline. The Fig. 2.5 shows the plot for real and imaginary part of visibilities. The average is taken for entire time of observation and the mean is taken separately for real and imaginary values and for two polarization.

Baseline calibration

Equation 2.2 contains the baseline-based gain term B_{ij} which is not antenna separable and therefore is cannot be corrected by self-calibration. AIPS has a task, BLCAL, to correct such baseline gains. However, baseline gain corrections are not constrained by the closure relations of self-calibration. Therefore, an incorrect application can seriously corrupt the data and artificially reduce the noise. We have investigated some of the possibilities of BLCAL, including transfer of gain solutions from the phase calibrator. While we have achieved significant improvement in the image noise, we are still in the process of understanding the consequences.

2.3.8 Summary of data reduction

Our data reduction was performed on all five days separately and for each sideband with 10 images in total. Following figures show the effect of each step of data reduction on the quality of the image.

The images labeled KZ1 and KZ8 in the Fig. 2.6 , represent the pre-selfcal

and the last self-calibration images. The imaged labeled LZ1 and LZ8 represent a similar series except that the flags identified in the KZ8 were transferred to LZ1. The noise levels of the four images are listed in Tab. 2.2

Table 2.2: List of image noise levels for selected images.

Image Name	Noise at the center μJy	Noise at corner μJy
GDNKZ1	186.9	49
GDNKZ8	37.5	24
GDNLZ1	125	47
GDNLZ8	30.8	25

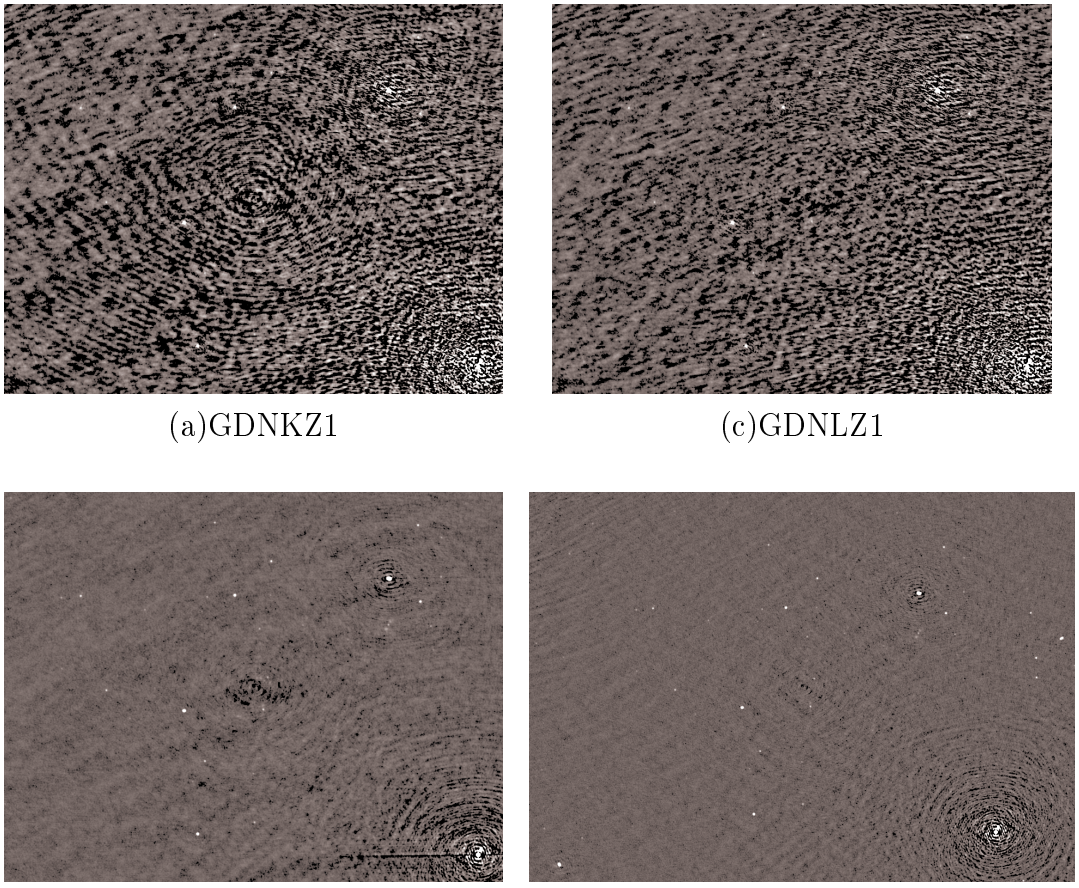

(a)GDNKZ1 (c)GDNLZ1

(b)GDNKZ8 (d)GDNLZ8

Figure 2.6: Representive sections of images (a) KZ1: First image made without self-calibration or flagging (b) KZ8: Image of KZ1 + self-calibration + flagging (c) LZ1 : KZ1 + flagging from KZ8. . (d) LZ8 : LZ1+ self-calibration + flagging

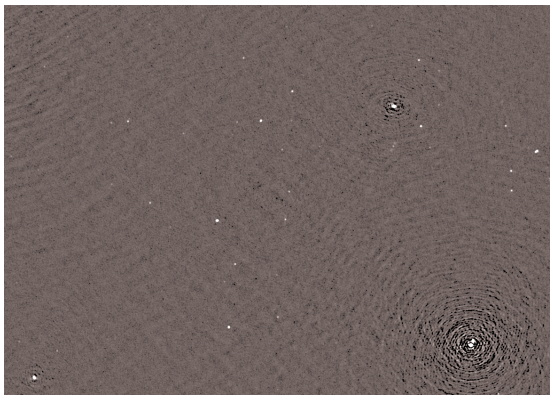

(a)GDNLZ18

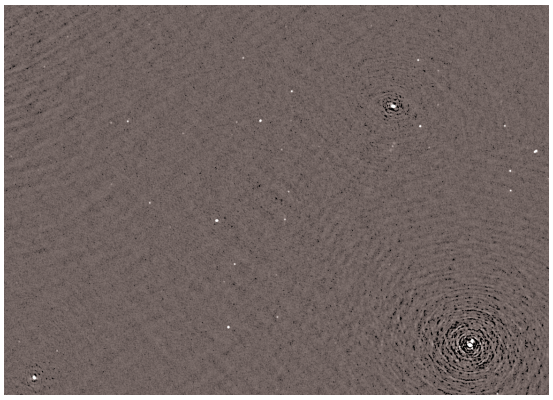

(b)GDNLZ19

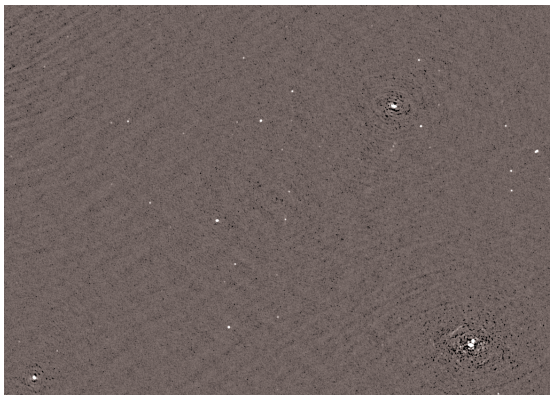

(c)GDNLZ21

Figure 2.7: Effect of baseline calibration using the AIPS task, BLCAL (a) LZ18 : Reference image (b) LZ19 : LZ18 + BLCAL using phase calibrator as a model.(c) LZ21 : LZ18 + BLCAL using the target field as a model. The noise levels were more or less the same. The spurious structures around strong sources reduced in LZ21.

Chapter 3

Results

The observed central frequency of 610 MHz corresponds to a redshift z = 1.73. The most distant OH maser detected [16, 2] has a line flux density of 8.4 mJy, corresponding to line luminosity of $10^4 L_\odot$ at a redshift z = 0.265. The same maser at z = 1.73, would have expected flux density of about 80μJy (Cosmological parameters used are H_o = 71 kms^{-1}Mpc^{-1}, Ω_M=0.27, Ω_λ = 0.73). We need to achieve a noise rms of 10μJy to detect such an emission line. Therefore, our attempt to detect the maser is within the limits of the possible though at the edge of it. However, this does require an extremely careful analysis to achieve the highest sensitivity possible.

After individually calibrating the data from each day we combined the visibilities from all days to make a single image per sideband. This yielded an image with rms noise of $\sim$ 12μJy, which is one of the deepest image ever made at 610 MHz. However, while carrying out the image quality checks, we realized that despite the very high sensitivity, there two issues which needed further attention.

1. There were still residual structures which we believe can be eliminated with more careful editing. This is critical to improve our chances of detecting a high redshift maser.

2. The flux densities of the sources on our image were lower than the expected values by a factor 1.7. The radio spectral index an important parameter for identifying the underlying physical process responsible for the radiation. Getting the flux density scale correct is extremely important for any scientific analysis.

One can easily correct for the discrepancy by scaling up the entire image by the factor 1.7. But this would mean that the achieved noise is 17μJy instead of 10μJy. Therefore, we feel that our scientific goals need a more careful understanding of the flux scaling discrepancy.

The rms noise level in the field is $\sim 30\mu$Jy. Now, we will combine data from all days into one to make a single image, this will reduce the noise by factor of $\sqrt{5} = 2.2$. We hope to reach noise level of $\sim 10\mu$Jy. The observed bandwidth (64MHz) covers redshift range of 1.59-1.88. The gigamaser with line luminosity of $10^4 L_\odot$ will produce a signal with an integrated flux within 66-100 μJy. Before continuing with spectral analysis, we have compared flux densities in our field for consistency with known surveys. It is important to check for such values, as wrong calibration parameters and flagging routines can alter visibilities in the data. One way to check for such errors is to compare best flux values with what is expected at that frequency.

3.1 Flux density scaling errors

GMRT is the only available instrument in the world at 610 MHz and there have been no other observations of GNF at this frequency. There was no direct way of comparing the correctness of our flux scale. Therefore, we used radio observations of the field at neighboring frequencies (straddling 610 MHz) to obtain an estimate of the flux densities of our detected sources.

The spectral index parametrizes the frequency variation of flux densities ac-

cording to the equation,

$$log\left(\frac{f_{\nu_1}}{f_{\nu_2}}\right) = \alpha\, log\left(\frac{\nu_1}{\nu_2}\right) \tag{3.1}$$

where f_{ν_1} and f_{ν_2} are flux densities at frequencies ν_1 and ν_2 respectively and α is the spectral index of the source.

We used the data from two radio surveys, Westerbork Northern Sky Survey (WENSS) [36] at 325 MHz and NRAO VLA Sky Survey (NVSS) [12] at 1.4 GHz. It should be noted that WENSS and NVSS have rms noise of 3.6 and 0.45 mJy respectively, which are about 100 times shallower than our image. So, most of our sources are not detected in WENSS and NVSS images.

There were 88 sources found in GNF from WENSS catalog and 385 sources were found from NVSS catalog. The correction to the response of primary beam was applied to the image using PBCOR. The source extraction in the target field was done using AIPS task SAD.

We detected a total of 390 sources in GNF at 610 MHz using AIPS task SAD. Of these only 27 had counterparts in the other two survey. Equation 3.1 was used to calculate the expected flux of these 27 sources at 610 MHz.

The fluxes of the sources are summarized in Tab. 3. Fig. 3.1 shows a plot of the flux ratio (expected/observed) against the observed flux density. We can see three main features in the plot.

1. There are many more objects at low flux densities than at high flux densities which is a well known fact.

2. The fractional error in the flux densities is much higher at lower flux densities. This is reflected in the larger scatter of points at low flux densities.

3. The four strongest sources have relatively more stable flux ratio. This is consistent with their fractional flux densities being smaller. The average

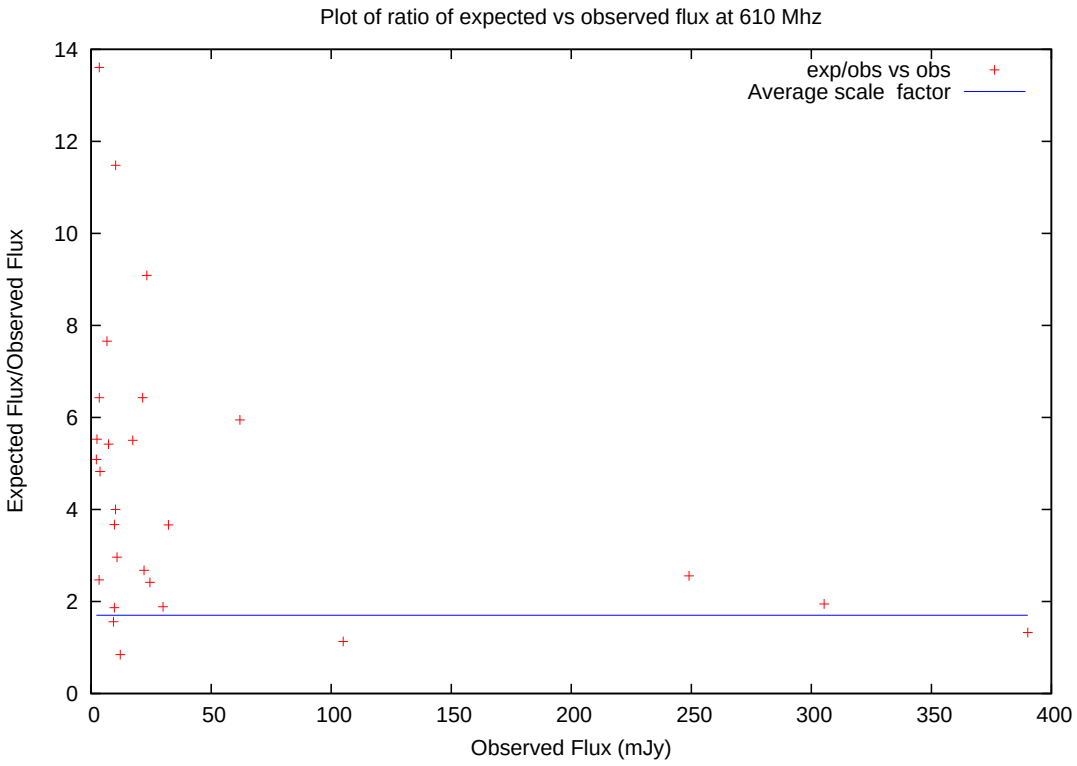

Figure 3.1: The plot of ratio of expected to observed flux at 610 MHz vs observed flux. The overall factor is around 1.7 for all fluxes. The large variation at low flux densities is due to noise.

ratio flux ratio for these sources is about 1.7 whereas it should have been 1, if flux scaling was correct.

We investigated several factors which may have contributed to this discrepancy.

The GMRT has a known elevation dependence of sensitivity which would change the measured flux density of a source. However, the phase calibrator only shows a 4% variation in flux density through the course of an observing session of 8 hours (See Tab. 3.2). Since, the phase calibrator and target field are very close to each other, we do not expect the elevation dependence of sensitivity to have caused the observed discrepancy.

Table 3.1: The summary of flux values

No.	RA h:m:sec	DEC ° :′:″	S_{325} mJy	S_{1400} mJy	Spectral index	S_{610} exp mJy	S_{610} obs mJy	exp/obs
1	12:31:23.710	+62:17:37.76	74	30.7	-0.60	50.6	6.6	7.66
2	12:31:30.012	+62:12:12.35	100	90.0	-0.07	95.6	17.4	5.50
3	12:31:54.314	+62:16:15.07	24	6.2	-0.93	13.4	2.4	5.53
4	12:32:05.280	+61:48:45.36	349	108.9	-0.80	211.2	23.2	9.09
5	12:32:27.002	+62:06:38.46	13	4.5	-0.73	8.2	3.3	2.47
6	12:32:47.074	+61:48:51.53	64	20.7	-0.77	39.3	7.3	5.42
7	12:33:36.226	+62:30:19.31	82	38.4	-0.52	59.1	24.5	2.42
8	12:34:09.115	+62:39:54.32	50	22.9	-0.53	35.7	9.7	3.67
9	12:34:11.606	+62:16:18.26	24	7.5	-0.80	14.5	9.3	1.56
10	12:34:51.658	+62:02:46.46	827	278.9	-0.74	517.6	390.2	1.33
11	12:35:38.203	+62:19:31.86	196	61.2	-0.80	118.7	105.0	1.13
12	12:35:55.150	+61:48:13.45	1095	265.4	-0.97	594.4	305.4	1.95
13	12:36:11.316	+62:33:15.75	25	11.9	-0.51	18.2	9.7	1.86
14	12:36:17.760	+62:47:29.81	32	13.4	-0.60	22.0	3.4	6.43
15	12:36:40.930	+62:40:04.75	104	28.1	-0.90	59.2	22.1	2.68
16	12:37:25.874	+62:11:29.40	18	4.9	-0.89	10.3	12.2	0.85
17	12:39:15.840	+62:00:17.64	94	28.8	-0.81	56.4	30.0	1.88
18	12:39:41.760	+62:32:05.28	50	17.7	-0.71	32.0	10.8	2.96
19	12:39:59.578	+61:33:42.85	49	42.2	-0.10	45.9	3.4	13.61
20	12:40:12.960	+62:26:27.60	1230	267.1	-1.05	636.7	249.0	2.56
21	12:40:30.720	+62:33:50.40	61	23.8	-0.64	40.7	10.2	4.00
22	12:40:59.040	+61:42:32.04	180	66.8	-0.68	117.4	10.2	11.48
23	12:41:05.712	+62:06:51.24	200	59.0	-0.84	118.2	32.2	3.66
24	12:41:07.937	+61:53:28.81	24	12.1	-0.47	17.9	3.7	4.83
25	12:41:09.134	+61:56:30.42	16	6.7	-0.60	11.0	2.2	5.09
26	12:41:11.520	+62:31:41.52	669	168.1	-0.95	368.8	62.0	5.95
27	12:41:47.990	+62:00:20.83	214	77.5	-0.70	138.1	21.5	6.43

Table 3.2: Flux densities of the phase calibrator, 1313+675, during an 8 hour observing session

	Upper-sideband	Lower-sideband
scan	total flux	total flux
	Jy	Jy
1	4.21	4.27
2	4.29	4.35
3	4.14	4.25
4	4.29	4.33

It is also possible that our absolute flux calibration scale was incorrect even while we managed to correct the temporal variation accurately. This would point to a incorrect transfer of scale from the flux calibrator to phase calibrator. However, we observed the flux calibrator four times during each session and all measurements were consistent with each other.

The primary beam pattern of GMRT is accurate only up to 10% away from the field center. Our flux ratio has been determined from only four sources which are all located away from the field center.

Five independent sessions of observations, spread across a month, in two different sidebands have yielded consistent flux densities for the sources in our field. This high degree of internal consistency coupled with a substantial discrepancy with other observations is very puzzling.

Chapter 4

Future plans

We believe that we have sufficient sensitivity and image analysis tools to detect OH megamasers at z = 1.7 if they are at least as luminous as the ones that have been discovered at low redshifts. It is known that the merging activity is higher at z > 1.[27] If the relationship between the far-IR luminosity (which is higher during mergers) and the maser line luminosity is continued to be true at high redshifts, it will greatly improve probability of detecting megamasers. The discovery of the new population of Submillimeter galaxies (SMG) [6, 22], has increased the expectation of detecting mega- and even gigamasers. The scientific rewards arising from a detection are very high.

We have reached very close to the required sensitivities. We expect to solve some of the image analysis issues in the near future. We plan to apply for a short observing run to the GMRT to settle the issue of flux scale.

Bibliography

[1] R. Athreya. A New Approach to Mitigation of Radio Frequency Interference in Interferometric Data. *ApJ*, 696:885–890, May 2009.

[2] W. A. Baan, J. Rhoads, K. Fisher, D. R. Altschuler, and A. Haschick. IRAS 14070 + 0525 - an OH gigamaser at z = 0.265. , 396:L99–L102, September 1992.

[3] W. A. Baan, P. A. D. Wood, and A. D. Haschick. Broad hydroxyl emission in IC 4553. *apjl*, 260:L49–L52, September 1982.

[4] A. H. Barrett, P. R. Schwartz, and J. W. Waters. Detection of Methyl Alcohol (CH_3OH) in Orion at λ ~ 1 cm. In *Bulletin of the American Astronomical Society*, volume 3 of *Bulletin of the American Astronomical Society*, page 388, June 1971.

[5] F. Biraud, G. Bourgois, J. Crovisier, R. Fillit, E. Gérard, and I. Kazès. OH observation of comet Kohoutek (1973f) at 18 cm wavelength. *NASA Special Publication*, 355:97–99, 1975.

[6] A. W. Blain, I. Smail, R. J. Ivison, J.-P. Kneib, and D. T. Frayer. Submillimeter galaxies. , 369:111–176, October 2002.

[7] R. S. Booth, R. P. Norris, N. D. Porter, and A. J. Kus. Observations of a circumstellar shell around the OH/IR star OH127.8-0.0. , 290:382–384, April 1981.

[8] J. A. Braatz, M. J. Reid, E. M. L. Humphreys, C. Henkel, J. J. Condon, and K. Y. Lo. The Megamaser Cosmology Project. II. The Angular-diameter Distance to UGC 3789. *apj*, 718:657–665, August 2010.

[9] C. Henkel and Braatz J.A. Megamasers. *Acta Astronomica Sinica Supplement Issue*, 44(55), Feb 2003.

[10] A. C. Cheung, D. M. Rank, C. H . Townes, D. D. Thornton, and W. J. Welch. *Nature*, 221:626, 1969.

[11] M. J. Claussen and K.-Y. Lo. Circumnuclear water vapor masers in active galaxies. *apj*, 308:592–599, September 1986.

[12] J. J. Condon, W. D. Cotton, E. W. Greisen, Q. F. Yin, R. A. Perley, G. B. Taylor, and J. J. Broderick. The NRAO VLA Sky Survey. , 115:1693–1716, May 1998.

[13] J. Darling. A Dense Gas Trigger for OH Megamasers. *apjl*, 669:L9–L12, November 2007.

[14] J. Darling and R. Giovanelli. A Search for OH Megamasers at Z $>$ 0.1. I. Preliminary Results. *aj*, 119:3003–3014, June 2000.

[15] J. Darling and R. Giovanelli. A Search for OH Megamasers at Z $>$ 0.1. II. Further Results. *aj*, 121:1278–1293, March 2001.

[16] J. Darling and R. Giovanelli. A Search for OH Megamasers at z $>$ 0.1. III. The Complete Survey. *aj*, 124:100–126, July 2002.

[17] M. Dickinson, M. Giavalisco, and GOODS Team. The Great Observatories Origins Deep Survey. In R. Bender and A. Renzini, editors, *The Mass of Galaxies at Low and High Redshift*, page 324, 2003.

[18] Moshe Elitzur. Physical characteristics of astronomical masers. *Rev. Mod. Phys.*, 54:1225–1260, Oct 1982.

[19] Moshe Elitzur. Astronomical masers. *Annual Review of Astronomy and Astrophysics*, 30(1):75–112, 1992.

[20] E. B. Fomalont and R. A. Perley. Calibration and Editing. In G. B. Taylor, C. L. Carilli, and R. A. Perley, editors, *Synthesis Imaging in Radio Astronomy II*, volume 180 of *Astronomical Society of the Pacific Conference Series*, page 79, 1999.

[21] J. R. Herrnstein, J. M. Moran, L. J. Greenhill, P. J. Diamond, M. Inoue, N. Nakai, M. Miyoshi, C. Henkel, and A. Riess. A geometric distance to the galaxy NGC4258 from orbital motions in a nuclear gas disk. , 400:539–541, August 1999.

[22] R. J. Ivison. Searching for a gigamaser in apm 08279+5255, and other short stories. *Monthly Notices of the Royal Astronomical Society*, 370(1):495–500, 2006.

[23] K. J. Johnston, S. R. Stolovy, T. L. Wilson, C. Henkel, and R. Mauersberger. VLA observations of the (N-15)H3 maser associated with NGC 7538 IRS 1. , 343:L41–L44, August 1989.

[24] N. Kanekar, C. L. Carilli, G. I. Langston, G. Rocha, F. Combes, R. Subrahmanyan, J. T. Stocke, K. M. Menten, F. H. Briggs, and T. Wiklind. Constraints on Changes in Fundamental Constants from a Cosmologically Distant OH Absorber or Emitter. *Physical Review Letters*, 95(26):261301, December 2005.

[25] C. Y. Kuo, J. A. Braatz, J. J. Condon, C. M. V. Impellizzeri, K. Y. Lo, I. Zaw, M. Schenker, C. Henkel, M. J. Reid, and J. E. Greene. The Megamaser Cosmology Project. III. Accurate Masses of Seven Supermassive Black Holes in Active Galaxies with Circumnuclear Megamaser Disks. *apj*, 727:20, January 2011.

[26] M. M. Litvak, A. L. McWhorter, M. L. Meeks, and H. J. Zeiger. Maser model for interstellar oh microwave emission. *Phys. Rev. Lett.*, 17:821–826, Oct 1966.

[27] K.Y. Lo. Mega-masers and galaxies. *Annual Review of Astronomy and Astrophysics*, 43(1):625–676, 2005.

[28] Philip Lockett and Moshe Elitzur. The Effect of 53 μm IR Radiation on 18 cm OH Megamaser Emission. *The Astrophysical Journal*, 677(2):985, 2008.

[29] E. Maoz. A Stringent Constraint on Alternatives to a Massive Black Hole at the Center of NGC 4258. *apjl*, 447:L91, July 1995.

[30] M. Miyoshi, J. Moran, J. Herrnstein, L. Greenhill, N. Nakai, P. Diamond, and M. Inoue. Evidence for a black hole from high rotation velocities in a sub-parsec region of NGC4258. , 373:127–129, January 1995.

[31] J. M. Moran, B. F. Burke, A. H. Barrett, A. E. E. Rogers, J. A. Ball, J. C. Carter, and D. D. Cudaback. The Structure of the OH Source in W3. *apjl*, 152:L97, May 1968.

[32] J. M. Moran and L. F. Rodriguez. Water-vapor masers and star formation in NGC 6334. , 236:L159–L163, March 1980.

[33] G. E. Morrison, F. N. Owen, M. Dickinson, R. J. Ivison, and E. Ibar. Very Large Array 1.4 GHz Observations of the GOODS-North Field: Data Reduction and Analysis. *apjs*, 188:178–186, May 2010.

[34] F. Perkins, T. Gold, and E. E. Salpeter. Maser Action in Interstellar OH. *apj*, 145:361, July 1966.

[35] Dos Santos PM and Lepine JRD. Detection of strong H_2O emission from galaxy NGC 4945. *Nature*, 278:615, 1979.

[36] R.B. Rengelink, Y. Tang, A.G. de Bruyn, G.K. Miley, M.N. Bremer, H.J.A. Röttgering, and M.A.R. Bremer. The westerbork northern sky survey (wenss). *Astron. Astrophys. Suppl. Ser.*, 124(2):259–280, 1997.

[37] M. J. Reid. Masers, from protostars to black holes: conference summary. In V. Migenes and M. J. Reid, editors, *Cosmic Masers: From Proto-Stars to Black Holes*, volume 206 of *IAU Symposium*, page 506, 2002.

[38] M. J. Reid, J. A. Braatz, J. J. Condon, L. J. Greenhill, C. Henkel, and K. Y. Lo. The Megamaser Cosmology Project. I. Very Long Baseline Interferometric Observations of UGC 3789. *apj*, 695:287–291, April 2009.

[39] M. J. Reid, J. A. Braatz, J. J. Condon, K. Y. Lo, C. Y. Kuo, C. M. V. Impellizzeri, and C. Henkel. The Megamaser Cosmology Project. IV. A Direct Measurement of the Hubble Constant from UGC 3789. *apj*, 767:154, April 2013.

[40] L. E. Snyder and D. Buhl. Detection of Possible Maser Emission Near 3.48 Millimeters from an Unidentified Molecular Species in Orion. , 189:L31–L33, April 1974.

[41] A. Tarchi. AGN and Megamasers. In R. S. Booth, W. H. T. Vlemmings, and E. M. L. Humphreys, editors, *IAU Symposium*, volume 287 of *IAU Symposium*, pages 323–332, July 2012.

[42] A. Tarchi, P. Castangia, C. Henkel, G. Surcis, and K. M. Menten. New H_2O masers in Seyfert and FIR bright galaxies. IV. Interferometric follow-ups. *aap*, 525:A91, January 2011.

[43] HAROLD WEAVER, DAVID R. W. WILLIAMS, and W. T. DIETER, N. H.and LUM. Observations of a strong unidentified microwave line and of emission from the oh molecule. *Nature*, 208:29–31, 1965.

[44] S. WEINREB, A H. Barrett, M. L. Meeks, and J. C. Henry. Radio observations of oh in the interstellar medium. *Nature*, 200(829), 1963.

[45] K. W. Willett. Searching for new OH megamasers out to redshifts z >1. In R. S. Booth, W. H. T. Vlemmings, and E. M. L. Humphreys, editors, *IAU Symposium*, volume 287 of *IAU Symposium*, pages 345–349, July 2012.

[46] Kyle William Willett. *OH Masers from Andromeda to the*. PhD thesis, University of Colorado, 2011.

[47] Zhang, J. S., Henkel, C., Guo, Q., and Wang, J. Radio properties of H2O maser host galaxies. *AA*, 538:A152, 2012.